ORDER, DISORDER, AND PHASE TRANSITION IN CONDENSED SYSTEM

Microstructure and Magnetooptics of Silicon Oxide with Implanted Nickel Nanoparticles

I. S. Edel'man[a,*], D. A. Petrov[a], R. D. Ivantsov[a], S. M. Zharkov[a,b], R. I. Khaibullin[c], V. F. Valeev[c], V. I. Nuzhdin[c], and A. L. Stepanov[c,d]

[a]*Kirensky Institute of Physics, Siberian Branch, Russian Academy of Sciences, Akademgorodok, Krasnoyarsk, 660036 Russia*
*e-mail: ise@iph.krasn.ru
[b]*Siberian Federal University, Svobodnyi pr. 79, Krasnoyarsk, 660041 Russia*
[c]*Zavoisky Physical-Technical Institute, Russian Academy of Sciences, Sibirskii trakt 10/7, Kazan, 420029 Russia*
[d]*Kazan (Volga Region) Federal University, ul. Kremlevskaya 18, Kazan, 420018 Russia*
Received April 28, 2011

Abstract—Metallic nickel nanoparticles of various sizes are formed in a thin near-surface layer in an amorphous SiO_2 matrix during 40-keV Ni^+ ion implantation at a dose of $(0.25-1.0) \times 10^{17}$ ions/cm^2. The microstructure of the irradiated layer and the crystal structure, morphology, and sizes of nickel particles formed at various irradiation doses are studied by transmission electron microscopy and electron diffraction. The magnetooptical Faraday effect and the magnetic circular dichroism in an ensemble of nickel nanoparticles are studied in the optical range. The permittivity $\hat{\varepsilon}$ tensor components are calculated for the implanted samples using an effective medium model with allowance for the results of magnetooptical measurements. The spectral dependences of the tensor $\hat{\varepsilon}$ components are found to be strongly different from those of a continuous metallic nickel film. These differences are related to a disperse structure of the magnetic nickel phase and to a surface plasma resonance in the metal nanoparticles.

DOI: 10.1134/S1063776111160035

1. INTRODUCTION

The demands for high-speed data recording, processing, and transmission optical devices stimulates searching for materials with high magnetooptical parameters [1, 2]. One of the promising ways for the development of this field is the creation of composite materials based on transition-metal nanoparticles. The excitation of conduction electrons in metal nanoparticles in the visible region of light waves changes the spectral dependences of the diagonal and off-diagonal components of a permittivity tensor, which can strongly modify magnetooptical spectra and increase the tensor components in a certain spectral region [3, 4]. Among the variety of methods used to form nanoparticles, high-dose ion implantation (ion synthesis mode) attracts particular attention due to the unlimited possibility of introducing any element of the periodic system into almost any matrix at a concentration that significantly exceeds the thermodynamic threshold of the impurity solubility. When the solubility threshold is exceeded, implanted impurity nanoparticles form in a thin near-surface layer in an irradiated substrate. Note that ion synthesis is widely used for the formation of various magnetic- or precious-metal nanoparticles in dielectric matrices to produce novel nanocomposite materials for magnetic recording or high-speed optical devices with extremely high non-

linear optical parameters (see reviews [5–9] and Refs. therein). Moreover, ion implantation synthesis of magnetic metal nanoparticles in dielectrics can be interesting not only for magnetic recording and nonlinear optics but also for producing novel combined magnetooptical materials.

Works dealing with magnetooptical phenomena, mainly the Kerr effect, in ion-synthesized nanocomposite materials are known. In particular, the authors of [10] studied the Kerr effect in an ensemble of nickel nanoparticles formed in an amorphous SiO_2 layer by implantation of negatively charged nickel ions. They observed both a substantial modification of the shape of Kerr rotation spectra and a strong change in the elliptical polarization of reflected light as compared to the data obtained for a continuous nickel film deposited onto an SiO_2 substrate. The Kerr effect spectra and the permittivity tensor components of nanocomposite layers were simulated in [10] using a modified Lissberger–Saunders approach [11], and qualitative agreement with experimental data was achieved in a spectral region up to 3 eV. In our earlier work [12], we presented the magnetic properties and the spectral dependences of the Faraday rotation angle (FRA) and the polar and longitudinal Kerr effects on of the cobalt impurity dose for an ensemble of cobalt particles created in an amorphous silicon dioxide matrix with ion

implantation. We found that the magnetooptical spectra of the formed nanocomposite materials differed substantially from those of continuous cobalt films. In this work, we continue to study the magnetooptical phenomena in SiO_2-based ion-synthesized nanocomposite materials. We now investigate dispersed nickel films synthesized by ion implantation at various doses. We measure the dispersion parameters of the ensembles of nickel nanoparticles formed in the near-surface layer of irradiated SiO_2, the magnetooptical FRA, and the magnetic circular dichroism (MCD), which have not been studied for ion-synthesized nickel nanoparticles. These results are compared to similar data obtained for thin continuous nickel films deposited onto an SiO_2 substrate.

2. EXPERIMENTAL

Magnetic nickel nanoparticles in an SiO_2 matrix were synthesized by the implantation of low-energy (40-keV) Ni^+ ions into parallel-sided plates of amorphous fused silica at a dose of 0.25×10^{17}, 0.5×10^{17}, 0.75×10^{17}, and 1.0×10^{17} ions/cm^2 (samples D1, D2, D3, and D4, respectively). Ion implantation was performed at room temperature on an ILU-3 ion-beam accelerator in a residual vacuum of 10^{-5} mmHg [13]. The current density in the ion beam was about $8\ \mu A/cm^2$. For comparison, we used thin continuous nickel films 17.5 and 20.5 nm thick produced by vacuum deposition.

The microstructure and phase composition of the implanted samples containing nickel nanoparticles were examined by transmission electron microscopy (TEM), electron diffraction (ED), and energy dispersive X-ray spectroscopy on a JEOL JEM-2100 (LaB6) transmission electron microscope at an accelerating voltage of 200 keV. These studies were carried out at the Electron Microscopy Laboratory of the Center for Joint Use of Siberian Federal University. The samples for electron-microscopic examination were prepared by a "transverse cut" method. Samples of the required thickness were prepared on a Gatan Precision Ion Polishing System (PIPS) by bombarding samples with 5-keV argon ions at an angle of 6° to the sample surface in vacuum. The FRA and MCD were measured using the normal geometry: the magnetic vector and the light beam direction were normal to the SiO_2 substrate plane. The contribution of the SiO_2 layers with implanted nickel to the FRA was determined as the difference between the spectra recorded for an irradiated sample and the initial SiO_2 matrix. The measured MCD spectra were caused only by nickel nanoparticles, since the transparent substrate did not contribute to this effect.

To measure the FRA, we used azimuthal modulation of the light wave polarization plane orientation. The measurement accuracy was ±0.2 min. Rotation angle α_F (reduced to effective sample thickness l) was measured in the spectral range 1.2–3.8 eV when an
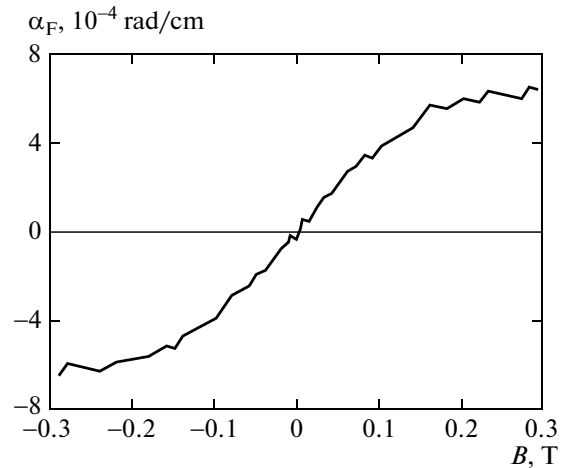
Fig. 1. Field dependence of the FRA α_F of the polarization plane in sample D4 at room temperature and a light wave energy of 2 eV. The magnetic field and the light wave propagation direction are normal to the sample surface.

applied magnetic field was changed from −0.3 to 0.3 T. In this magnetic field, the samples implanted by the maximum doses exhibited saturation characteristic of an ensemble of superparamagnetic nanoparticles (Fig. 1, sample D4).

When measuring the MCD, we used modulation of the state of light wave polarization from the right-hand to the left-hand circular polarization. The modulator represented a fused silica prism with a glued piezoceramic element. When an ac signal of frequency ω, which corresponds to the natural frequency of the system, is supplied to the piezoceramic element, an elastic standing wave is excited in the quartz plate. In the absence of an acoustic excitation, a prism is optically isotropic. When a compression half-wave passes through it, the acoustic excitation propagation direction (along the horizontal prism axis) becomes a "slow" prism axis. When the second half-wave, namely, a tension half-wave, passes through the prism, the picture changes into the reverse one: the tension axis becomes a "fast prism axis. If linearly polarized light, whose polarization plane is rotated through an angle of 45° to the horizontal prism axis, is incident on the prism, the light at the exit from the prism is circularly polarized when a standing acoustic wave is excited in it. This polarization changes from a right-hand to a left-hand circle at the acoustic vibration frequency of the prism. If a sample exhibits the MCD effect, the absorption coefficients of the light waves polarized along right-hand and left-hand circles with respect to the magnetic moment of the sample are different; as a result, the light flux having passed through the sample and reaching a photomultiplier has a modulated intensity. The constant component of the photomultiplier flux was maintained at the same level during a change in the light wavelength; therefore, the variable signal at the exit from the photomultiplier was
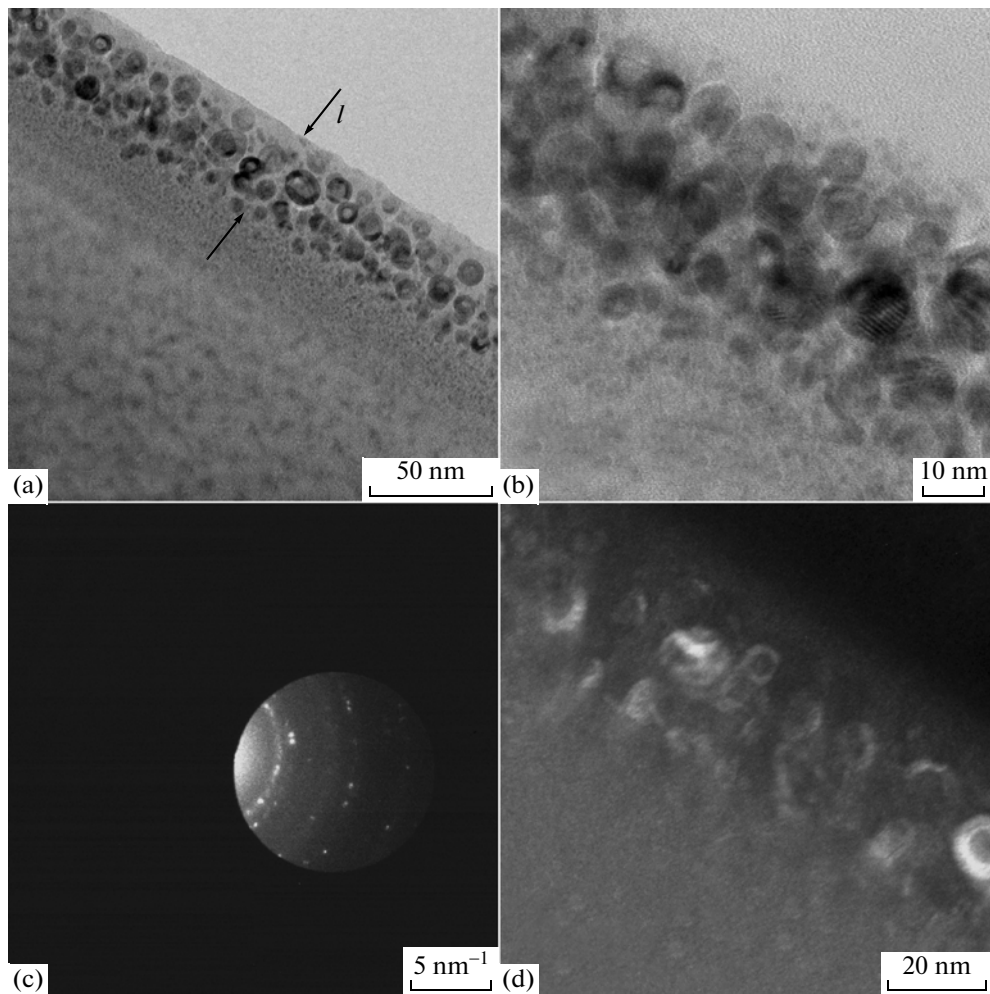
Fig. 2. (a, b) Bright-field images, (c) electron diffraction pattern taken with a selector aperture, and (d) corresponding dark-field image of the cross section of sample D4.

proportional to the magnitude of MCD. The MCD effect was measured as the difference between two signals for two opposite directions of an applied magnetic field. The absolute value of MCD was calibrated with the technique described in [14], and MCD was measured in the spectral range 1.1–4.2 eV in a magnetic field of 0.35 T at room temperature. The measurement accuracy was 10^{-4}, and the spectral resolution was 20–50 cm^{-1} depending on the wavelength. The MCD spectra of sample D3 implanted at a dose of 0.75×10^{17} ions/cm^2 were also recorded in the temperature range 95–300 K.

3. ELECTRON-MICROSCOPIC EXAMINATION

Using TEM and ED, we studied the transverse sections of samples D3 and D4 implanted at rather high doses. As an example, Fig. 2 shows the microstructure and phase composition of the transverse section of sample D4.

Nickel particles are observed as dark spots in bright-field images (Figs. 2a, 2b) and as bright spots in dark-field images (Fig. 2d). The shape of nickel particles is close to a circular shape in electron micrographs taken at different angles of sample inclination (from 0° to 30°). Therefore, the nickel nanoparticles having formed in the implanted region in SiO$_2$ have a spherical shape. The ion-synthesized nickel particles lie at a depth of 10–15 nm from the sample surface in a thin layer, which is 30 nm thick in sample D3 and 40 nm in sample D4. The total thickness of the modified region in SiO$_2$ is the same in both cases, 65 nm. The elemental composition determined by energy dispersive X-ray spectroscopy supports the presence of nickel in the irradiated layer and its absence outside the implantation-modified region in SiO$_2$.

The diffraction reflections in the electron diffraction pattern shown in Fig. 2c correspond to an fcc structure (space group $Fm3m$) with a lattice parameter $a = 3.52$ Å. This structure is characteristic of bulk
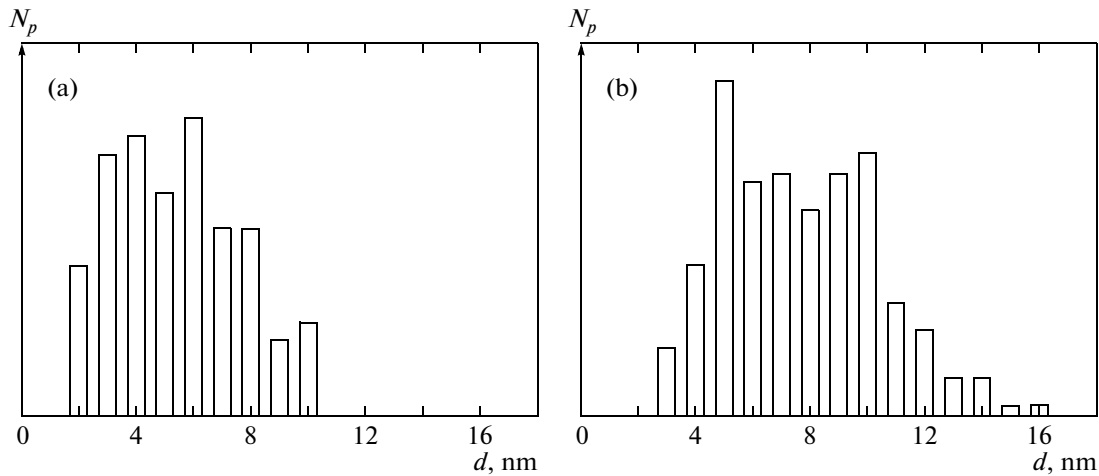
Fig. 3. Diameter d distribution of nickel particles for samples (a) D3 and (b) D4.

nickel. Moiré fringes with a period of about 1 nm are observed in some electron-microscopic images when nickel particles are overlapped (e.g., Fig. 2b). Moiré fringes are known to appear when two regular crystal lattices are juxtaposed, and these lattices should have either different periods or be rotated with respect to each other. Thus, the formation of Moiré fringes indicates that the nickel nanoparticles have a regular crystal structure.

Figure 3 shows the size d distributions of nickel particles N_p in samples D3 and D4. As follows from these distributions, the ion-synthesized spherical nickel particles have a diameter of 2–10 nm in sample D3 and 3–16 nm in sample D4.

4. MAGNETOOPTICAL EFFECTS

The spectral dependences of FRA in a continuous 17.5-nm-thick nickel film and in samples D2–D4 containing implanted nickel nanoparticles are shown in Fig. 4 (data for sample D1 implanted at the minimum dose are not shown because of its weak signals). It is seen that spectral curves *2–4* of samples D2–D4 differ from the FRA spectrum of the continuous nickel film, which fully corresponds to the data in [15]: the spectral dependences of the implanted samples have a pronounced FRA maximum, which shifts from 3.35 to 2.88 eV when the implantation dose increases, and the sign of the effect changes at 2.00, 1.85, and 1.71 eV for samples D2, D3, and D4, respectively. For the nickel film, the FRA is positive over the entire spectral range under study, is maximal at 1.25 eV, and has a weak local maximum near 2.5 eV.

Similarly to the FRA spectra, the MCD spectra of the implanted samples (θ, which is the magnitude of MCD divided by the effective film thickness, was measured) differ substantially from the spectrum of the continuous nickel film (Fig. 5). The MCD spectra of

samples D2–D4 (curves *2–4*) have two pronounced extrema: a positive maximum shifts from 3.65 to 3.50 eV when the implantation dose increases, and a negative (in sign) maximum (i.e., minimum in the spectral dependence) also shifts toward low energies as the dose increases. The spectral position of the negative MCD maximum approximately corresponds to the range of a change in the sign of FRA (i.e., passage through zero), which shifts toward the high-energy spectral region by 0.2–0.3 eV depending on the dose. On the other hand, the position of the FRA maximum corresponds to the passage through zero in the spectral dependence of MCD. This correspondence between the FRA and MCD spectra is retained up to 3.5 eV. The correspondence between the position of the max-
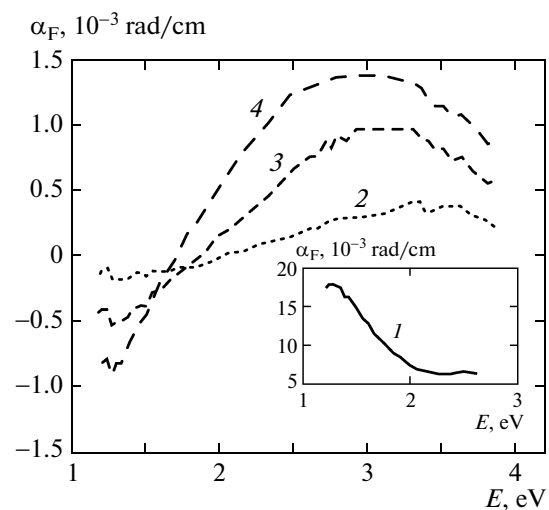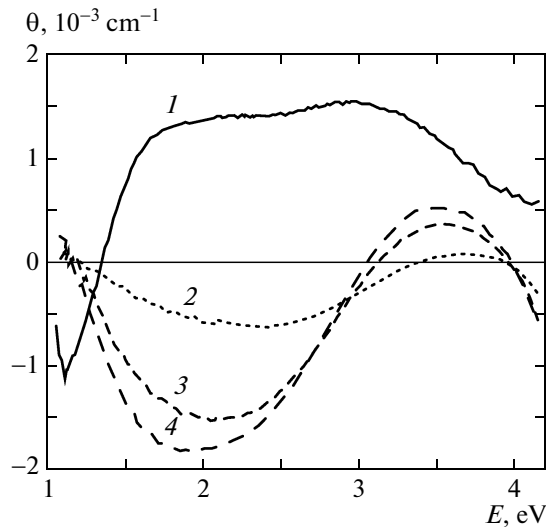

Fig. 4. Spectral dependences of FRA in (*2–4*) samples D2–D4, respectively, in a field of 0.29 T. (*1*) The spectral dependence of FRA for a continuous 17.5-nm-thick nickel film in the same field.

θ, 10^{-3} cm^{-1}

Fig. 5. Spectral dependences of MCD for (*1*) continuous 20.5-nm-thick nickel film and (*2–4*) implanted samples D2–D4, respectively, in a field of 0.35 T.

imum in the FRA spectrum and the point of a change in the sign (passage through zero) near 1 eV in the MCD spectrum is also observed for a continuous nickel film.

The signal amplitude increases monotonically with the implantation dose for both magnetooptical effects, which is explained by an increase in the quantity of the magnetically ordered nickel phase in the implanted SiO$_2$ layer. We estimated the specific FRA (the angle of rotation of polarization plane divided by the effective ferromagnetic layer thickness) in sample D4 by making allowance for the thickness of the layer containing nickel nanoparticles (Fig. 2a) and its filling with the magnetic phase. Our estimation demonstrates that the specific FRA at the maximum of the spectral dependence of sample D4 is close to the specific FRA in a continuous nickel film in the given spectral region.

A decrease in the sample temperature to 95 K leads to an increase in MCD at the extreme points by approximately 20% and to an insignificant shift of the extrema toward high energies. Note that a decrease in MCD with decreasing temperature significantly exceeds the increase in the spontaneous magnetization of bulk nickel in this temperature range (see, e.g., Fig. 17.2 in [16]).

5. DISCUSSION OF RESULTS

From a phenomenological viewpoint, the magnetooptical effects in any material result from the effect of an applied magnetic field or its magnetization on complex permittivity ε of the material, which characterizes the response of the medium to an electromagnetic field [17]. Thus, to discuss the nature of the detected phenomena, we have to determine the tensor

$\hat{\varepsilon}$ components in the samples under study as functions of the implantation dose or the filling with a ferromagnetic phase. In the simplest case of an isotropic material magnetized along axis z, tensor $\hat{\varepsilon}$ is described by the relationship

$$\hat{\varepsilon} = \begin{bmatrix} \varepsilon_{xx} & i\varepsilon_{xy} & 0 \\ -i\varepsilon_{xy} & \varepsilon_{yy} & 0 \\ 0 & 0 & \varepsilon_{zz} \end{bmatrix}, \tag{1}$$

where $\varepsilon_{xx} = \varepsilon_{yy}$. The real ($\varepsilon'_{xx}$) and imaginary ($\varepsilon''_{xx}$) parts of component ε_{xx} are related to complex refractive index $\eta = n - ik$, which is measured experimentally, by the expressions

$$\varepsilon'_{xx} = n^2 - k^2,$$
$$\varepsilon''_{xx} = 2nk, \tag{2}$$

where n is the refractive index and k is the absorption coefficient; this coefficient is related to absorption coefficient α, which is usually measured from the ratio of the intensities of light incident on a sample and having passed through the sample, by the formula $\alpha = 2k\omega/c$, where ω is the frequency and c is the velocity of light. The real and imaginary parts of off-diagonal component ε_{xy} are usually determined using the experimental values of the magnetooptical effects. The transverse Kerr effect is traditionally used for this purpose (see, e.g., [18]). However, the Kerr effect spectra of the implanted samples can be distorted by the contribution of reflections from the boundaries of a transparent matrix. Therefore, we use the recorded FRA and MCD spectra to find ε_{xy}. The complex FRA of a homogeneous ferromagnet is described by the expression [19]

$$\alpha_F - i\theta = \frac{\pi}{\lambda}(\eta_+ - \eta_-)l, \tag{3}$$

where α_F and θ are the angle of rotation in FRA and the magnitude of MCD divided by effective sample thickness l, respectively, and λ is the incident light wavelength, and η_+ (η_-) is the complex refraction index for a wave with the right (left) circular polarization relative to the magnetic field direction. We take into account the fact that
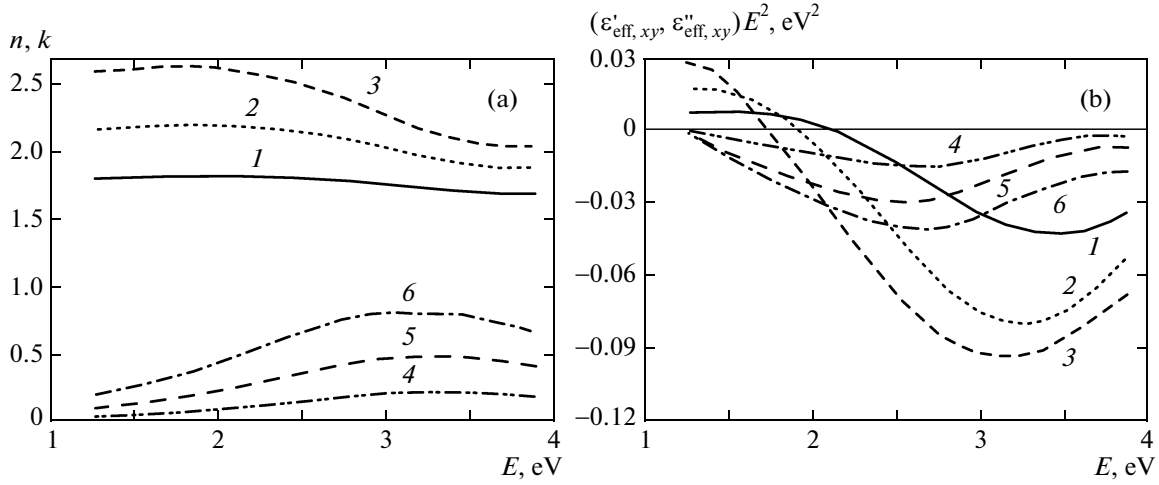
$$\eta_+ - \eta_- = \varepsilon_{xy}/\sqrt{\varepsilon_{xx}}, \tag{4}$$

and have

$$a_F - i\theta = \frac{\pi}{\lambda}l\frac{\varepsilon_{xy}}{\sqrt{\varepsilon_{xx}}}. \tag{5}$$

After rather simple transformations, we obtain the following expressions for α_F and θ:

$$\alpha_F = -\frac{\pi}{\lambda}\left(\frac{k}{k^2+n^2}\varepsilon''_{xy} + \frac{n}{k^2+n^2}\varepsilon'_{xy}\right), \tag{6}$$

Fig. 6. (a) Spectral dependences of the effective values of coefficients (*1–3*) n and (*4–6*) k calculated for samples D2–D4, respectively, by Eq. (10). (b) Spectral dependences of the off-diagonal components of the effective permittivity tensor ($\varepsilon'_{\mathrm{eff},\,xy}$ + $\varepsilon''_{\mathrm{eff},\,xy}$)$E^2$ ((*1–3*) $\varepsilon'_{\mathrm{eff},\,xy}E^2$, (*4–6*) $\varepsilon''_{\mathrm{eff},\,xy}E^2$) calculated for samples D2–D4 by Eqs. (8) and (9), respectively, with allowance for the experimental data obtained for α_F and θ and the calculated values of n and k.

$$\theta = \frac{4\pi}{\lambda}\left(\frac{n}{k^2+n^2}\varepsilon''_{xy} - \frac{k}{k^2+n^2}\varepsilon'_{xy}\right). \qquad (7)$$

From these expressions, we have

$$\varepsilon'_{xy} = -\frac{\lambda}{\pi}\left(n\alpha_\mathrm{F} + \frac{k\theta}{4}\right), \qquad (8)$$

$$\varepsilon''_{xy} = -\frac{\lambda}{\pi}\left(n\alpha_\mathrm{F} - \frac{n\theta}{4}\right). \qquad (9)$$

Equations (8) and (9) were employed earlier in [20] to determine the off-diagonal tensor $\hat{\varepsilon}$ components of yttrium iron garnet using experimentally measured FRA and MCD.

The substantial differences between the FRA and MCD spectra of the implanted samples and a continuous nickel film are thought to be caused by the dispersed structure and the in-depth distribution of the magnetic nickel phase in an implanted SiO_2 matrix. More specifically, spherical nickel nanoparticles in the implanted samples are buried in a thin near-surface layer of the irradiated dielectric. Note that such differences between the magnetooptical spectra of homogeneous and dispersed samples of a certain metal were repeatedly detected earlier (see, e.g., [10, 21–24]).

To describe the optical and magnetooptical properties of dielectric media with embedded metallic nanoparticles, researchers usually apply the effective medium approximation, which was introduced by Maxwell-Garnett at the beginning of the last century [25] and then developed and improved by many authors (see, e.g., [3, 11, 26]). In this approximation, a medium containing heterogeneities much smaller than the light wavelength is described by effective tensor $\hat{\varepsilon}_\mathrm{eff}$, which is similar to tensor $\hat{\varepsilon}$ for the corresponding homogeneous medium, and, correspondingly, by effective refractive and absorption indices. In essence, the tensor $\hat{\varepsilon}_\mathrm{eff}$ components represent an averaged combination of the optical parameters of metallic particles and the parent matrix. With this approach, we calculated the spectral dependences of the real and imaginary parts of diagonal effective tensor component $\varepsilon_{\mathrm{eff},\,xx}$ for samples D2–D4 using the formula [3, 10]

$$\varepsilon_{\mathrm{eff},\,xx} = \varepsilon'_{\mathrm{eff},\,xx} + i\varepsilon''_{\mathrm{eff},\,xx}$$
$$= \varepsilon_d\frac{\varepsilon_{xx}(1+2p) + 2\varepsilon_d(1-p)}{\varepsilon_{xx}(1-p) + \varepsilon_d(2+p)}, \qquad (10)$$

where ε_d is the permittivity of the quartz matrix, ε_{xx} is the diagonal component of the permittivity tensor of bulk nickel, and p is the filling of the irradiated layer with the metal obtained from an analysis of electron-microscopic images (see Fig. 2a). The real and imaginary components of ε_{xx} of bulk nickel were determined using the spectra of coefficients n and k of continuous nickel films presented in [27], and the optical constants of the particle material were assumed to be equal to the constants of bulk nickel. The spectra of $\varepsilon_{\mathrm{eff},\,xx}$ thus obtained were then used to determine the spectra of coefficients n and k for samples D2–D4 by Eq. (2). Off-diagonal components $\varepsilon_{\mathrm{eff},\,xy}$ were calculated by Eqs. (8) and (9) using calculated coefficients n and k and the experimental data for quantities α_F and θ (see Figs. 4, 5). The calculation results are shown in Fig. 6.

Figure 6a shows the spectral dependences of refractive index n and absorption coefficient k of the media of nanocomposite samples D2–D4 containing implanted nickel nanoparticles. These calculated dependences of both coefficients differ substantially

from those of bulk nickel [27]. This is especially true of the $k(E)$ dependence: a broad maximum in the spectral range 3.2–3.5 eV appears in it. The position of this maximum shifts toward low energies when filling factor p increases. In the model used in this work, spectra $n(E)$ and $k(E)$ approach those of bulk nickel as factor p increases and coincide with them in the limiting case at $p = 1$.

To verify the model for sample D3, we recorded the optical absorption spectrum; the shape of this spectrum was found to resemble the $k(E)$ spectrum calculated for this sample and had a much worse resolution of the maximum. It should be noted that the experimental absorption spectra of ion-implanted samples can be substantially distorted because of multiple incoherent reflections from the surfaces of a dielectric matrix in the form of a parallel-sided plate [28]; therefore, the use of them to obtain information on the processes occurring in metallic nanoparticles can be incorrect. The authors of [29] used a technique that was thought to exclude such reflections from matrix boundaries and detected a maximum centered at 3.3 eV in the absorption spectrum of an SiO_2 sample implanted by negative Ni^- ions at an energy of 60 keV, a current of 56 μA/cm², and a dose of 3.8×10^{16} ion/cm². They attributed this maximum to the excitation of a surface plasma resonance (SPR), i.e., the collective electron excitation induced by an applied field [30–35], in nickel nanoparticles. An applied ac electric field (the electric component of an electromagnetic wave incident on a sample) with a wavelength much larger than the particle size acts on the valence electrons and ions making up a nanoparticle. Since the ion mass is larger than the electron mass by three orders of magnitude, the ions remain almost immovable and the electrons shift from their equilibrium positions. This leads to the formation of uncompensated charges on the nanoparticle surface and the appearance of a restoring force; as a result, an electron cloud begins to oscillate with respect to its equilibrium position. Thus, the term "surface plasmons" reflects the fact that, although electrons oscillate with respect to positively changed ions throughout the particle, surface polarization is the main restoring force. These collective excitations are characterized by a finite lifetime and a certain frequency, which differs substantially from the plasma frequency in the corresponding bulk material; as a result, the spectra of optical absorption and magnetooptical effects change. Mie was the first to formulate the problem of the excitation of surface plasmons as far back as 1908 [32, 36, 37]. He solved the Maxwell equations with boundary conditions for an ensemble of metallic nanoparticles distributed in a dielectric matrix provided that the particle size is small as compared to the light wavelength and interparticle interaction is absent and derived the following expression for the coefficient of light absorption in such a system:

$$k(\omega) = \frac{9\omega \varepsilon_d^{3/2} V}{c} + \frac{\varepsilon_{xx}''(\omega)}{\left[\varepsilon_{xx}'(\omega) + 2\varepsilon_d\right]^2 + \varepsilon_{xx}''(\omega)^2}, \quad (11)$$

where ω is the applied electromagnetic field frequency and $V = 4\pi a^3/3$ is the particle volume. An absorption (i.e., SPR) resonance should take place when the denominator in Eq. (11) is minimal. For alkali metals, Mie proposed the following simplified expression for SPR frequency ω_M:

$$\omega_M = \frac{\omega_p}{\sqrt{\varepsilon_d + 2\varepsilon_{xx}'}}, \quad (12)$$

where $\omega_p = \sqrt{4\pi n_e e^2/m_e}$ is the plasma frequency of the bulk metal and ε_{xx}' is the permittivity of the metal without regard for the contribution of free carriers. The latter is described by the well-known Drude formula [38]

$$\varepsilon_e(\omega) = 1 - \frac{\omega_p^2}{\omega^2 + i\omega\omega_\tau}, \quad (13)$$

where ω_τ is the relaxation frequency. However, it was shown in [39] that the SPR frequency in the case of nickel can be correctly determined only by Eq. (11).

Numerous experimental investigations of SPR in nanoparticles of alkali metals (see, e.g., [40]) and, then, precious metals [41] showed that the SPR frequency is well below the frequency following from the Mie theory [30, 40, 42, 43]. This discrepancy is usually ascribed to the spill-out effect, i.e., a change in the electron density near a particle surface [30–32]. The electron density in small particles at $T = 0$ K is determined by a multiparticle wavefunction of the ground state. However, this function propagates outside the geometric volume of a particle, which is determined by its radius, and some electrons N_{out} turn out to be outside the particle. According to [31], the spill-out effect leads to the following expression for the SPR frequency:

$$\tilde{\omega}_M \approx \omega_M - \frac{\omega_M}{2}\frac{N_{out}}{N}, \quad (14)$$

where N is the total number of electrons. Thus, the SPR shifts toward the long-wavelength region of the spectrum as compared to the Mie resonance. The N_{out}/N ratio is determined by the ratio of external electron cloud volume V_{out} to the total volume, $V_{out}/(V_{out} + V)$. Here, V is the physical particle volume and V_{out} is the volume of the sphere around the particle into which electrons spill.

In addition, there are other effects influencing the SPR frequency. Nevertheless, to estimate the SPR frequency in the system of nanoparticles under study (which is rather far from an ideal system to be considered theoretically), we restrict ourselves to determining quantities ω_M and $\tilde{\omega}_M$ using Eqs. (12) and (14), respectively. It is seen from Eq. (11) that frequency ω_M

is only determined by the dielectric parameters of the matrix and the particle material. The authors of [39] obtained $\omega_M = 3.47$ eV for nickel nanoparticles in an SiO_2 matrix using the spectral dependences of refractive index n and absorption coefficient k of bulk nickel from [27]. Since we used the same matrix (SiO_2) and were based on the data in [27] to calculate the dielectric parameters, the value of ω_M obtained in this work coincides with that in [39]. To take into account the spill-out effect using Eq. (14), we assume that volume V_{out} is equal to the volume of the sphere around a 0.5-nm-thick particle, which is close to the nickel lattice parameter. Then, for an average particle diameter of 8 nm in sample D4, we have

$$\frac{V_{out}}{V_{out} + V} \approx 0.3, \quad \tilde{\omega}_M \approx 3 \text{ eV}.$$

Near 3 eV, i.e., in the vicinity of the SPR frequency, we detected a change in the sign of MCD for all samples (see Fig. 5). The shape of the MCD spectra can be explained by the spin splitting of the electron plasma oscillation frequencies and different densities of electrons with opposite spin directions. This situation is schematically shown in Fig. 7 for sample D3, where the MCD spectrum is represented as the difference between two absorption bands. The absorption band amplitudes are taken to be equal to the amplitudes of the positive and negative components in the MCD spectrum. As shown in Fig. 2c in [44], this procedure is justified if the splitting exceeds the band width. The envelope of the bands has a maximum at a frequency $\tilde{\omega}_M \approx 3$ eV, which corresponds to the estimated SPR frequency. The band width is caused by both attenuation processes and a significant scatter of the particle sizes. It is now impossible to separate these two mechanisms.

Figure 6b shows the calculated spectra of the real and imaginary parts of the off-diagonal tensor $\hat{\varepsilon}_{eff}$ component. The off-diagonal components of tensor $\hat{\varepsilon}$ for bulk nickel were calculated in a number of works using the measurement of the Kerr effect in the visible light wavelength region (see [18] and review [45] and Refs. therein). The calculation results obtained in different works are close to each other with insignificant discrepancies. The spectral dependences of $\varepsilon_{eff, xy}$ calculated in this work differ substantially from the corresponding spectra of bulk nickel. The main characteristic feature of the spectra of both parts (real and imaginary) of the off-diagonal component of tensor $\hat{\varepsilon}_{eff}$ is the presence of broad maxima in the optical range. In this case, the maximum for real part $\varepsilon_{eff, xy}'$ shifts toward low energies when the dose (amount of introduced nickel) increases, the maximum in the spectrum of absorption coefficient k behaves similarly, and the centers of gravity of the maxima in the spectral
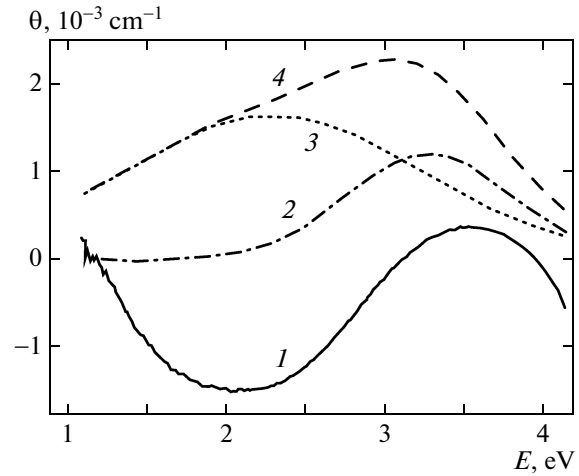
Fig. 7. Decomposition of the MCD spectrum of sample D3 into components: (*1*) experimental spectrum of MCD; (*2, 3*) absorption bands calculated so that their difference is equal to MCD and their sum is the optical absorption coefficient (curve *4*).

dependences of $\varepsilon_{eff, xy}'$ and k coincide at the same implantation dose.

In an order of magnitude, the values of $\varepsilon_{eff, xy}'$ for the implanted samples are comparable with the values of ε_{xy}' for bulk nickel and thin continuous nickel films [45]. The value of $\varepsilon_{eff, xy}''$ for the implanted samples is an order of magnitude lower than the value of ε_{xy}'' for bulk nickel. The absolute values of $\varepsilon_{eff, xy}'$ and $\varepsilon_{eff, xy}''$ increase with the implantation dose. In contrast to the spectrum of $\varepsilon_{eff, xy}'$, the spectrum of $\varepsilon_{eff, xy}''$ does not shift when the dose changes.

Thus, the main contribution to FRA and MCD for an ensemble of ion-implanted nickel nanoparticles in an SiO_2 matrix in the visible region is mainly related to the excitation of SPR in the metal nanoparticles.

6. CONCLUSIONS

Using TEM of the transverse section of a sample, we showed that high-dose implantation of fast Ni^+ ions into an amorphous fused silica (SiO_2) substrate results in the formation of spherical metallic nickel nanoparticles in the implanted surface layer. The ion-implanted nickel nanoparticles have an fcc structure, and their sizes vary from 2 to 16 nm depending on the implantation dose (amount of introduced magnetic nickel). In the spectral range 1.2–3.8 eV, we studied the effect of the implantation dose on the magnetooptical MCD and FRA in a composite SiO_2 layer containing implanted nickel nanoparticles. The shape of the magnetooptical spectra in the composite layer was

found to be strongly modified as compared to the FRA and MCD spectra of a continuous nickel film.

In particular, the spectral dependences of SiO_2 samples containing nickel nanoparticles have pronounced FRA and MCD maxima, which shift with the implantation dose, and the signs of both magnetooptical effects change. Based on the results of magnetooptical measurements, we used an effective medium model to calculate the complex permittivity tensor components of the samples. The calculated positions of the maxima in the $\varepsilon'_{\mathrm{eff},\,xy}$ and k spectra in the range 3.5−3.2 eV are related to SPR excitation in ion-synthesized nickel nanoparticles, and the scatter of the particle sizes explains the maximum width. Thus, the specific features of the spectral dependences of the FRA and MCD in an ensemble of nickel nanoparticles implanted into an SiO_2 matrix that were detected in the optical range are mainly determined by the SPR excitation in nickel nanoparticles rather than intraband electron transitions, as in the case of a continuous nickel film.

ACKNOWLEDGMENTS

REFERENCES

1. N. A. Tolstoi and A. A. Spartakov, *Electrooptics and Magnetooptics of Disperse Systems* (St. Petersburg State University, St. Petersburg, 1996) [in Russian].

2. A. K. Zvezdin and V. V. Kotov, *Modern Magnetooptics and Magnetooptical Materials* (Institute of Physics, London, 1997).

3. T. K. Xia, P. M. Hui, and D. Stroud, J. Appl. Phys. **67**, 2736 (1990).

4. E. A. Gan'shina, M. V. Vashuk, A. N. Vinogradov, A. B. Granovsky, V. S. Gushchin, P. N. Shcherbak, Yu. E. Kalinin, A. V. Sitnikov, Chong-Oh Kim, and Cheol Gi Kim, JETP **98** (5), 1027 (2004).

5. A. Meldrum, R. F. Haglund, L. A. Boatner, and C. W. White, Adv. Mater. (Weinheim) **13**, 1431 (2001).

6. F. Gonella, Rev. Adv. Mater. Sci. **14**, 134 (2007).

7. R. I. Khaibullin, B. Z. Rameev, A. L. Stepanov, C. Okay, V. A. Zhikharev, I. B. Khaibullin, L. R. Tagirov, and B. Aktas, in *NATO Science Series II: Mathematics, Physics and Chemistry*, Vol. 143: *Nanostructured Magnetic Materials and Their Applications*, Ed. by B. Aktas, L. Tagirov, and F. Mikailov (Kluwer, Dordrecht, 2004), p. 33.

8. A. L. Stepanov, *Ion-Synthesis of Silver Nanoparticles and Their Optical Properties* (Nova Science, New York, 2010).

9. A. L. Stepanov, in *Silver Nanoparticles*, Ed. by D. P. Perez (In-tech, Vukovar, Croatia, 2010), p. 93.

10. H. Amekura, Y. Takeda, and N. Kishimoto, Thin Solid Films **464−465**, 268 (2004).

11. P. H. Lissberger and P. W. Saunders, Thin Solid Films **34**, 323 (1976).

12. I. S. Edelman, O. V. Vorotynova, V. A. Seredkin, V. N. Zabluda, R. D. Ivantsov, Yu. I. Gatiyatova, V. F. Valeev, R. I. Khabullin, and A. L. Stepanov, Phys. Solid State **50** (11), 2088 (2008).

13. A. L. Stepanov and I. B. Khaibullin, Rev. Adv. Mater. Sci. **9**, 109 (2005).

14. G. K. Kostyuk, E. K. Galanov, and M. V. Leikin, Opt.-Mekh. Prom-st., No. 5, 28 (1976).

15. H. Clemens and J. J. Jaumann, Z. Phys. **173**, 135 (1963).

16. S. V. Vonsovskii, *Magnetism* (Nauka, Moscow, 1971; Wiley, New York, 1974).

17. L. D. Landau and E. M. Lifshitz, *Course of Theoretical Physics*, Vol. 8: *Electrodynamics of Continuous Media* (Fizmatlit, Moscow, 2003; Butterworth−Heinemann, Oxford, 2004).

18. G. S. Krinchik and V. A. Artem'ev, Sov. Phys. JETP **26** (6), 1080 (1967).

19. A. V. Sokolov, *Optical Properties of Metals* (Fizmatgiz, Moscow, 1961; Elsevier, New York, 1967).

20. G. B. Scott, D. E. Lacklison, H. I. Ralph, and J. L. Page, Phys. Rev. B: Solid State **12**, 2562 (1975).

21. E. Ganshina, A. Granovsky, V. Gushin, M. Kuzmichov, P. Podrugin, A. Kravetz, and E. Shipil, Physica A **241**, 45 (1997).

22. E. A. Gan'shina, M. V. Vashuk, A. N. Vinogradov, A. B. Granovsky, V. S. Gushchin, P. N. Shcherbak, Yu. E. Kalinin, A. V. Sitnikov, Chong-Oh Kim, and Cheol Gi Kim, JETP **98** (5), 1027 (2004).

23. S. Ozaki, H. Kura, H. Maki, and T. Sato, J. Appl. Phys. **105**, 113913 (2009).

24. C. Clavero, A. Cebollada, G. Armelles, Y. Huttel, J. Arbiol, F. Peiró, and A. Cornet, Phys. Rev. B: Condens. Matter **72**, 024441 (2005).

25. J. C. Maxwell-Garnett, Philos. Trans. R. Soc. London, Ser. A **203**, 358 (1904).

26. M. Abe and M. Gomi, Jpn. J. Appl. Phys. **23**, 1580 (1984).

27. P. B. Johnson and R. W. Christy, Phys. Rev. B: Solid State **9**, 5056 (1974).

28. Y. Takeda, V. T. Gritsyna, N. Umeda, C. G. Lee, and N. Kishimoto, Nucl. Instrum. Methods Phys. Res., Sect. B **148**, 1029 (1999).

29. H. Amekura, Y. Takeda, and N. Kishimoto, Nucl. Instrum. Methods Phys. Res., Sect. B **222**, 96 (2004).

30. W. A. de Heer, Rev. Mod. Phys. **65**, 611 (1993).

31. M. Brack, Rev. Mod. Phys. **65**, 677 (1993).

32. U. Kreibig and M. Vollmer, *Optical Properties of Metal Cluster* (Springer, Berlin, 1995), p. 23.

33. *Springer Series in Chemical Physics*, Vol. 52: *Clusters of Atoms and Molecules I*, Ed. by H. Haberland (Springer, Berlin, 1994).

34. *Springer Series in Chemical Physics*, Vol. 56: *Clusters of Atoms and Molecules II*, Ed. by H. Haberland (Springer, Berlin, 1994).

35. G. F. Bertsch and R. A. Broglia, *Oscillations in Finite Quantum Systems* (Cambridge University Press, Cambridge, 1994).

36. G. Mie, Ann. Phys. (Leipzig) **25**, 377 (1908).

37. M. Born and E. Wolf, *Principles of Optics: Electromagnetic Theory of Propagation, Interference and Diffraction of Light* (Cambridge University Press, Cambridge, 1959; Nauka, Moscow, 1973).

38. N. W. Ashcroft and N. D. Mermin, *Solid State Physics* (Harcourt, Orlando, Florida, United States, 1976).

39. O. A. Yeshchenko, I. M. Dmitruk, A. A. Alexeenko, and A. M. Dmytruk, J. Phys. Chem. Solids **69**, 1615 (2008).

40. C. Bréchignac, P. Cahuzac, J. Leygnier, and A. Sarfati, Phys. Rev. Lett. **70**, 2036 (1993).

41. S. Dhara, B. Sundaravel, T. R. Ravindran, K. G. M. Nair, C. David, B. K. Panigrahi, P. Magudapathy, and K. H. Chen, Chem. Phys. Lett. **399**, 354 (2004).

42. C. Bréchignac, P. Cahuzac, N. Kebaïli, J. Leygnier, and A. Sarfati, Phys. Rev. Lett. **68**, 3916 (1992).

43. T. Reiners, C. Ellert, M. Schmidt, and H. Haberland, Phys. Rev. Lett. **74**, 1558 (1995).

44. N. V. Starostin and P. P. Feofilov, Sov. Phys.—Usp. **12** (2), 252 (1969).

45. Š. Višňovský, V. Pařízek, M. Nývlt, P. Kielar, V. Prosser, and R. Krishnan, J. Magn. Magn. Mater. **127**, 135 (1993).

Translated by K. Shakhlevich